



## ORIGINAL ARTICLE

# Graphene quantum dot composite with multiphoton excitation as near infrared-II probe in bioimaging



Wen-Shuo Kuo<sup>a,b,1</sup>, Yen-Sung Lin<sup>c,d,1</sup>, Meng-Zhi Han<sup>c,1</sup>, Hao-Yu Chuang<sup>e,f</sup>,  
Ping-Ching Wu<sup>g</sup>, Chia-Yuan Chang<sup>h</sup>, Jiu-Yao Wang<sup>b</sup>, Hui-Fan Kao<sup>i</sup>,  
Shih-Wen Tseng<sup>j</sup>, Sheng-Han Lin<sup>k,\*</sup>, Po-Lan Su<sup>l,\*</sup>, Chan-Chi Chang<sup>m,\*</sup>

<sup>a</sup> School of Chemistry and Materials Science, Nanjing University of Information Science and Technology, Nanjing 210044, Jiangsu, China

<sup>b</sup> Center for Allergy Immunology and Microbiome (AIM), China Medical University Children's Hospital/China Medical University Hospital, China Medical University, Taichung 404, Taiwan

<sup>c</sup> Division of Pulmonary and Critical Care Medicine, An Nan Hospital, China Medical University, Tainan 709, Taiwan

<sup>d</sup> Department of Nursing, Chung Hwa University of Medical Technology, Tainan 717, Taiwan

<sup>e</sup> Cell Therapy Center | Department of Neurosurgery, An Nan Hospital, China Medical University, Tainan 709, Taiwan

<sup>f</sup> Department of Neurosurgery, China Medical University Beigang Hospital, Yunlin County 651, Taiwan

<sup>g</sup> Department of Biomedical Engineering, National Cheng Kung University, Tainan 701, Taiwan

<sup>h</sup> Department of Mechanical Engineering, National Cheng Kung University, Tainan 701, Taiwan

<sup>i</sup> Department of Nursing, National Tainan Junior College of Nursing, Tainan 700, Taiwan

<sup>j</sup> Core Facility Center of National Cheng Kung University, National Cheng Kung University, Tainan 701, Taiwan

<sup>k</sup> Department of Anesthesiology, E-Da Hospital, I-Shou University, Kaohsiung 840, Taiwan

<sup>l</sup> Department of Internal Medicine, National Cheng Kung University Hospital, College of Medicine, National Cheng Kung University, Tainan 701, Taiwan

<sup>m</sup> Department of Otolaryngology, National Cheng Kung University Hospital, College of Medicine, National Cheng Kung University, Tainan 701, Taiwan

Received 16 May 2023; accepted 19 July 2023

Available online 25 July 2023

## KEYWORDS

Biocomposites;  
Nonlinear laser;  
Near-infrared-II nano-probe;

**Abstract** Non-radiative traps and structures are present on the graphene quantum dots doped with nitrogen and functionalized with amino groups (amino-N-GQDs) and multiple crystalline layers because of cross-link-enhanced emission. Secondary and tertiary amines, which are potential fluorophores, have also been observed on the polyethylenimine (PEI) coating of amino-N-GQDs.

\* Corresponding authors.

E-mail addresses: [ed111667@edah.org.tw](mailto:ed111667@edah.org.tw) (S.-H. Lin), [polan.750317@gmail.com](mailto:polan.750317@gmail.com) (P.-L. Su), [109a0015@gs.ncku.edu.tw](mailto:109a0015@gs.ncku.edu.tw) (C.-C. Chang).

<sup>1</sup> The authors contributed equally to this work.

Peer review under responsibility of King Saud University.



## Two-photon excitation; Bioimaging

Cross-linked PEI coating reduced rotation and vibration, thereby enhancing the photoluminescence quantum yield (PL QY). Introduced nitrogen atoms from N dopants, amino-functionalized groups and PEI, as well as sulfur from polystyrene sulfonate (PSS) enhanced the cooperative effect on the properties of heteroatom-doped materials among electrons captured by new surface states. This enhanced radiative recombination and subsequently enhanced PL QY, therefore, surface conjugation improved the amino-N-GQD surfaces by increasing the quantum confinement of their emissive energy, evidenced by the increased PL QY of amino-N-GQD-PSS-PEI (or amino-N-GQD-polymer composites). In some situations, the maximum available power required for delivery to the two-photon imaging plane without damaging tissues limits imaging depth but the additional brightness provided by amino-N-GQD-polymer composites in this study extended the maximum imaging depth to 240  $\mu\text{m}$ . Amino-N-GQD-polymer composites had favorable two-photon properties under two-photon excitation (self-developed femtosecond Ti-sapphire laser optical system; power: 23.93 nJ pixel<sup>-1</sup>, 160 scans, approximately 1.09 s of total exposure time; excitation wavelength: 980 nm, near-infrared-II region), indicating that cells treated with amino-N-GQD-polymer composites and the anti-epidermal growth factor receptor antibody can achieve two-photon luminescence with 1/81 of the power required for similar-intensity two-photon autofluorescence (1938.33 nJ pixel<sup>-1</sup> with 800 scans, total exposure time of  $\sim$ 5.44 s). The materials can serve as contrast agents for the non-invasive detection of biological specimens and interior tissues using a two-photon excitation wavelength in the near-infrared region.

© 2023 The Authors. Published by Elsevier B.V. on behalf of King Saud University. This is an open access article under the CC BY-NC-ND license (<http://creativecommons.org/licenses/by-nc-nd/4.0/>).

## 1. Introduction

Materials fabricated at the nanometer scale are sensitive to size reductions and shape changes. Currently, graphene-based nanoparticles are widely employed in biological applications because they offer excellent biocompatibility and stability (Torres et al., 2017). Alternate graphene nanostructures are required in biomedical applications principally because such applications require near-infrared (NIR) light that inherently exhibits deep tissue penetration; however, this light is less absorbed than other types of radiation. NIR laser excitation can be used to achieve optimal tissue transmission because it has a low degree of scattering and energy absorption. Therefore, the NIR region provides the highest possible irradiation penetration for target tissue and reduces autofluorescence and photobleaching for non-target tissue, thereby enabling the observation or investigation of thick tissue and deep specimens. NIR-absorbing graphene-based nanostructures have numerous biological applications, in particular, graphene quantum dot (GQD)-based materials can be applied in photodynamic therapy and bioimaging (Kuo et al., 2020).

GQD materials have large surface areas in addition to strong surface grafting that involves  $\pi$ - $\pi$  conjugations and the groups present on the surface of such materials may be the origin of new phenomena associated with defect- and intrinsic-state emissions (Sun et al., 2020). Such new phenomena may involve photoluminescence (PL) with intrinsic-state emission induced by localized electron-hole pair recombination, the quantum size effect, and edge sites with zigzag shapes, whereas defect-state emission is caused by defect effects (energy traps) (Kuo et al., 2020). The degree of quantum energy confinement on carbon-based material surfaces can be increased through a surface passivation reaction between oligomeric poly(ethylene glycol) diamine and poly(propionylethyleneimine-co-ethyleneimine). Increased quantum confinement engenders high PL and quantum yield (QY) in such materials (Yang et al., 2021). The same phenomenon can be triggered by the surface-passivated reactions of polymers containing sulfur (S) and nitrogen (N) (Kumar et al., 2022). The integrity of networks of surface  $\pi$  electrons can be increased through surface passivation, which can also prevent localized electron-hole pairs from undergoing non-radiative recombination. Both situations increase the QY of GQD-based materials (Dsouza et al., 2021, Kang et al., 2021). Non-radiative traps and structures present on the carbon core of the crystalline amino-N-GQDs with multiple crystalline layers, secondary

and tertiary amines, which are potential fluorophores, were observed on the polyethylenimine (PEI) because of cross-link-enhanced emission (Baman et al., 2018). The cross-linked PEI painted on the materials reduced rotation and vibration, thereby enhancing PL (Baman et al., 2018), potentially achieving a high QY. The introduced S and N atoms augment the cooperative effect exerted on the properties of the heteroatoms-doped materials among the electrons captured by the new surface states, thereby enhancing radiative recombination and the QY (Dsouza et al., 2021, Kang et al., 2021, Kumar et al., 2022, Yang et al., 2021). Therefore, surface conjugation improved the materials' surfaces by increasing the quantum confinement of their emissive energy; this quantum confinement was measured in terms of the increased QY of amino-N-GQD-polymer composites.

Studies have examined the luminescence induced by one-photon excitation (OPE) continuous-wave lasers but few studies have addressed the use of illuminated GQD-based materials combined with multiphoton excitation to develop contrast agents (Liao et al., 2012, Yang et al., 2022). Multiphoton microscopy, also known as two-photon excitation (TPE) laser microscopy, is a popular imaging modality and a laser-scanning microscopy technique that induces fluorescence through localized non-linear excitation. In bioimaging, multiphoton microscopy is typically employed in tandem with NIR-I and NIR-II non-linear lasers excitation to maximize tissue transmission (Feng et al., 2021). Additionally, multiphoton microscopy requires a short photoexcitation period and has extremely low energy requirements, therefore, it is an alternative bioimaging technique (Lee et al., 2019). Accordingly, the development of a highly photostable and biocompatible probe for a GQD-based material that considerably reduces the laser power required for imaging is paramount for the general application of TPE laser microscopy.

## 2. Materials and methods

### 2.1. Preparation of GQD-based materials

GQDs: Graphene oxide was prepared using a natural graphite powder (Bay Carbon Inc., Bay City, MI, USA) through a modified Hummers' method (Hummers et al., 1958). Graphite (8.5 M) and NaNO<sub>3</sub> (0.6 M) (Merck & Co., Kenilworth, NJ, USA) were mixed with H<sub>2</sub>SO<sub>4</sub> (FUJIFILM Wako Chemicals

USA Inc., Richmond, VA, USA).  $\text{KMnO}_4$  (2.0 M, FUJIFILM Wako Chemicals USA Inc.) was slowly added with continual stirring at 35 °C (Corning, New York, NY, USA) overnight. Subsequently, deionized water ( $\text{ddH}_2\text{O}$ ) was gradually added and continually stirred before  $\text{H}_2\text{O}_2$  (35%; Sigma Aldrich Co., St Louis, MO, USA) was added to terminate the reaction. The graphene oxide was washed several times with  $\text{ddH}_2\text{O}$  before it was collected and placed in a tube furnace (Tainan, Taiwan) and heated to 400–600 °C in the presence of argon for 4–6 h. Concentrated  $\text{HNO}_3$  (16.0 M, Sigma Aldrich Co.) was added and stirred for 2 d. The mixture was placed in a water bath sonicator (Rocker Scientific Co. Ltd., New Taipei City, Taiwan) for 2 d at 45°, then placed in an oven at 160 °C (Yotec Instruments Co. Ltd., Hsinchu City, Taiwan) for 1 d to vaporize all the liquid. Washing and centrifugation (approximately 847,200 RCF, > 10 min; Optima TLX Ultracentrifuge, Beckman Coulter Inc., Brea, CA, USA) with  $\text{ddH}_2\text{O}$  were conducted several times before the supernatant was filtered through a 0.22  $\mu\text{m}$  microporous membrane (Nylon filter membrane, Merck & Co.). The pH (7.4; Hanna Co. Ltd., Thane, Maharashtra, India) of the resulting black suspension was adjusted with NaOH (Sigma Aldrich Co.) to obtain the GQDs specimens.

GQDs doped with nitrogen (N-GQDs): Graphene oxide was prepared from a natural graphite powder using a modified Hummers' method. Graphite (8.5 M) and  $\text{NaNO}_3$  (0.6 M) were mixed with  $\text{H}_2\text{SO}_4$  and  $\text{KMnO}_4$  was slowly added with continual stirring at 35 °C overnight. Subsequently,  $\text{ddH}_2\text{O}$  was gradually added and continually stirred before the reaction was terminated with  $\text{H}_2\text{O}_2$ . Several washing and centrifugation steps with  $\text{ddH}_2\text{O}$  were performed and the graphene oxide was collected. The as-prepared graphene oxide was placed in a tube furnace and heated to 400–600 °C in the presence of ammonia (Sigma Aldrich Co.) for 4–6 h before the addition of concentrated  $\text{HNO}_3$  (16.0 M) and stirred for 2 d. The mixture was placed in a water bath sonicator for 2 d at 45 °C, then placed in an oven at 160 °C for 1 d to vaporize all the liquid. Washing and centrifugation (approximately 847,200 RCF, > 10 min) with  $\text{ddH}_2\text{O}$  were performed several times before the supernatant was filtered through a 0.22  $\mu\text{m}$  microporous membrane. The pH (7.4) of the resulting black suspension was adjusted with NaOH to obtain the N-GQDs.

GQDs doped with N and functionalized with amino groups (amino-N-GQDs): The as-prepared N-GQDs were mixed with ammonia, stored in a Teflon-lined stainless steel autoclave, and reacted at 180 °C for 5 h. The resulting mixture was washed with  $\text{ddH}_2\text{O}$ , centrifuged several times, and subsequently dried in an oven at 50 °C overnight to obtain the amino-N-GQDs.

The 0.1  $\text{mg mL}^{-1}$  or 1.0  $\text{mg mL}^{-1}$  stock solutions were prepared for the following experiments.

### 2.2. Femtosecond laser optical system (for fluorescence lifetime imaging microscopy, FLIM)

The self-made femtosecond Ti-sapphire laser (a repetition rate of 80 MHz; Mai Tai with the optical parametric oscillators, Spectra-Physics, USA; Scheme S1) was used and FLIM were used according to the previous studies (Kuo et al., 2020, Kuo et al., 2020). The lifetime data and parameter are generated using the triple-exponential equation fitting [3 exp fitting

model:  $a_0 \cdot \exp(a_1x) + a_2 \cdot \exp(a_3x) + a_4 \cdot \exp(a_5x) + a_6$ ] while monitoring the emission under TPE (Ex: 980 nm).

All materials and methods for this article can be found in the [Supplementary Material](#).

## 3. Results

### 3.1. Characterization of materials

Graphene oxide sheets were prepared by a modified Hummers method to fabricate GQDs via an ultrasonic shearing reaction (Hummers et al., 1958). Nitrogen (N) was used to dope the GQDs, which were then functionalized with an amino group to produce amino-N-GQDs. Low-magnification transmission electron microscopy (TEM; Fig. 1a) and high-magnification high-resolution TEM (HR-TEM; Fig. 1b) were used to determine the mean size of the amino-N-GQDs in the lateral dimension ( $7.1 \pm 0.6$  nm) as well as their size distribution (Table S1). The interlayer spacing of the derived amino-N-GQDs was 0.213 nm (Fig. 1b), which could be attributed to the  $d$ -spacing  $\{1\ 1\ \bar{0}0\}$  present in graphene lattice fringes. The height profiles of the materials were determined through atomic force microscopy (AFM), indicating a single  $1.00 \pm 0.03$ -nm-thick layer of amino-N-GQDs (Fig. S1a). Hydroxyl, amino, and epoxy groups were exposed on the amino-N-GQDs, as revealed by Fourier-transform infrared spectroscopy (Fig. S1b). Therefore, the surface charge was approximately 13.6 mV, as evidenced by zeta-potential spectroscopy. An absorption peak was identified at approximately 225 nm corresponding to the aromatic C=C bonds'  $\pi$ - $\pi^*$  transition. The C-N and C=O shoulder's  $n$ - $\pi^*$  transitions appeared at  $\sim 323$  nm, indicating  $\pi$  electron transition in the oxygen-containing amino-N-GQDs. This also confirmed the N doping of the dots, as revealed by ultraviolet-visible (UV-Vis) spectroscopy (Fig. S1c). The D- and G-band (located at  $\sim 1384$  and  $1606$   $\text{cm}^{-1}$ , respectively) integrated intensity ratio ( $I_D/I_G$ ) in the Raman spectrum was approximately 0.90, indicating high-quality samples. The amino-N-GQDs had higher disorder and distortion (Fig. 1c; Fig. S1d) than graphite (0.104) (Wu et al., 2012). The  $I_D/I_G$  values were used to determine the GQD specimens' mean  $\text{sp}^2$ -domain size (Sheka et al., 2020), which was similar in the Raman and HR-TEM calculations but the Raman calculations ( $\sim 6.9$  nm) slightly underestimated the size because the Raman estimation (Kuo et al., 2020) [Equations (S10-S11), Supplementary Material] ignores the oxygenated regions. X-ray diffraction (XRD) showed the diffraction angle of amino-N-GQDs peaked broadly at  $\sim 24.3^\circ$ , which means an interlayer distance of 0.360 nm (Fig. S1e). XPS to analyze the deconvoluted C(1 s) spectra revealed C-C/C=C (285.8 eV), C-N (286.8 eV), C-O (287.2 eV), and C=O (288.1 eV) bonds in addition to functional groups containing oxygen. The ratio of O(1 s) to C(1 s) was approximately 31%. The deconvoluted N(1 s) spectra revealed relevant details of C-N bonding. The samples treated with ammonia contained pyridinic (398.2 eV), amino (398.9 eV), pyrrolic (399.8 eV), quaternary (400.8 eV), and amide (O=C-N, 401.2 eV) N functional groups (Figs. 1d & e; Fig. S1f). The N functionality composition [5.3% of N(1 s)/C(1 s)] was obtained using the deconvoluted N(1 s) spectra, indicating that the hydrothermal ammonia treatment

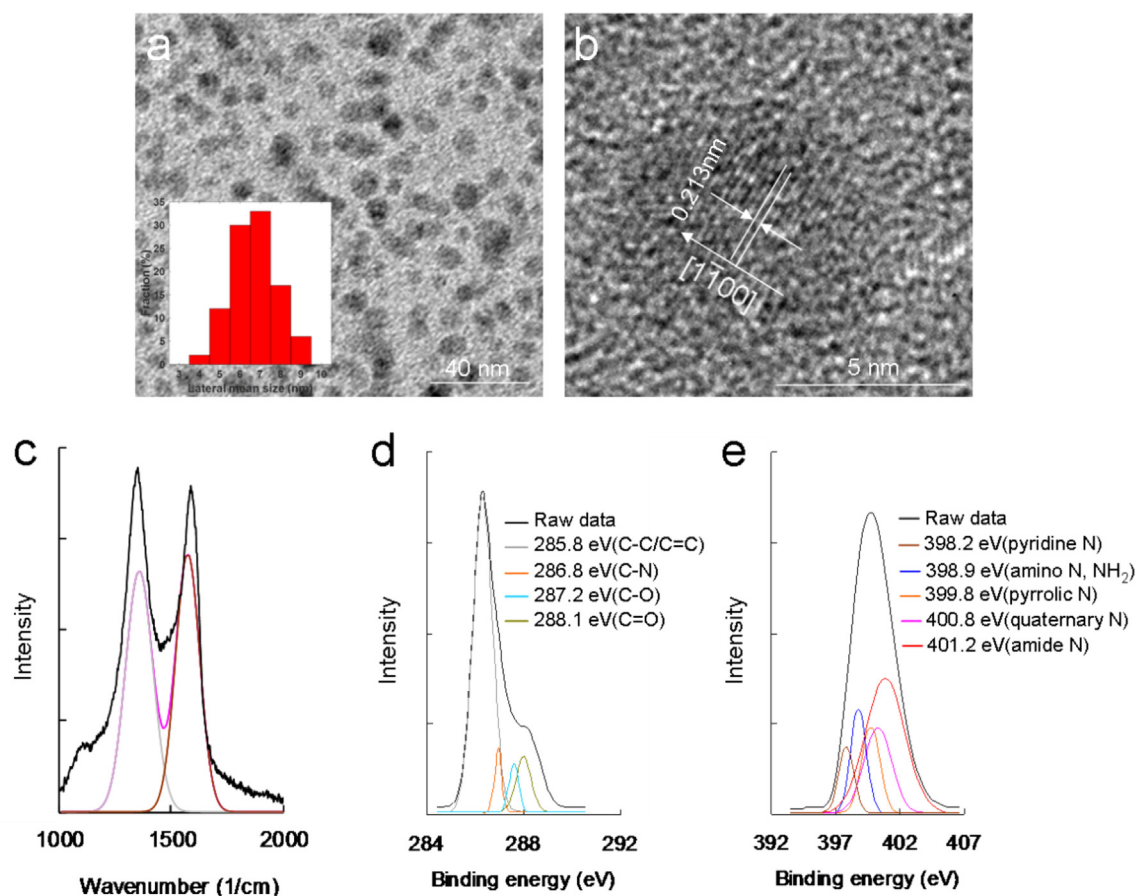


**Fig. 1** (a) Low-magnified TEM image [inset: Quantitative size distribution was determined by DLS. Cell type: DTS1060C; Measurement duration: 30 number of runs, 20 run duration (sec)]; (b) HR-TEM image of a single amino-N-GQD with d-spacing of 0.213 nm. (c) Amino-N-GQD Raman spectrum decomposed and fitted to D-band (gray line) and G-band (brown line) peaks (at  $\sim 1384$  and  $\sim 1606$   $\text{cm}^{-1}$ , respectively; pink line: decomposed spectrum; black line: raw data). (d and e) Deconvoluted XPS spectra of C(1s) with peaks for C-C/C=C, C-N, C-O, and C=O. Spectra and XPS peaks for N(1s) of pyridinic N, amino N ( $\text{NH}_2$ ), pyrrolic N, quaternary N, and amide N ( $\text{O}=\text{C}-\text{N}$ ). The Gaussian function was used to fit the peaks. Other XPS findings are presented in Fig. S1f (Supplementary Material). Material dose:  $1 \mu\text{g mL}^{-1}$ .

caused N atom substitutional doping forming quaternary, pyrrolic, and pyridinic N functionalities (Fig. 1e; Fig. S1f) and some carbonyl and epoxy group moieties were converted into amide and amino functionalities, respectively. In graphene oxide-based materials, electron orbital resonance patterns are affected by N functionalities. Some aromatic rings may be damaged by the ammonia annealing treatment, so when graphene oxide is subjected to ultrasonic exfoliation and cutting in nitric acids, such aromatic ring damage may have engendered defective peripheral carbonyl and pyrrolic groups. The product was subsequently treated with hydrothermal ammonia, which may have converted carbonyl groups to amide groups on the amino-N-GQDs. Fig. S1g presents a conceptual diagram of an amino-N-GQD. These experimental details confirm the successful preparation of amino-N-GQDs.

### 3.2. Nitrogen dopant, amino functionalization, and polymer conjugation

For phototherapy, the intrinsic properties of GQD-based materials can be modified with N dopants to markedly change

the carrier density, resulting in electrical and optical properties that are completely distinct from their intrinsic counterparts. N-doped GQD-based materials have remarkable electrochemical, photochemical, and electrocatalytic activities which are advantageous in optoelectronic and biomedical applications (Kuo et al., 2020). The efficient engineering of graphene structure band gaps and local chemical features can be achieved by doping them with heteroatoms to modify their optical properties and electronic characteristics (Zhang et al., 2023). Some promising contrast agents for bioimaging have limited practical applicability because carbon-based materials have an insufficient QY for such applications. However, the QY can be efficiently increased by heteroatom doping, surface passivation, or both. Polystyrene sulfonate (PSS) and polyethylenimine (PEI) were used to paint the amino-N-GQD surfaces in the present study. These GQDs were N-doped as well as amino-functionalized through an electrostatic interaction with the PSS and PEI to establish whether the PL and QY could be enhanced. Some details of the successful characterizations of amino-N-GQD-PSS-PEI (or amino-N-GQD-polymer composites) are illustrated in Figs. S2–S5. There were approximately 11,642 PSS and approximately 25,991 PEI coated on

the surfaces of each amino-N-GQD and amino-N-GQD-PSS, respectively (Fig. S6). For the amino-N-GQDs, the relative QY for Cy5.5 in dimethyl sulfoxide [for reference,  $QY_{\text{ref}} = 0.28$  (Li et al., 2012)] was 0.30, whereas the relative QYs for amino-N-free GQDs (0.17) and amino-group-free N-GQDs (0.22) were not favorable (Fig. S7). Similar absolute QYs (Ruhlandt et al., 2020) of 0.16, 0.21 and 0.30 for amino-N-free GQDs, amino-group-free N-GQDs and amino-N-GQDs were obtained. Electrostatic interaction was used to deposit a coating of PSS followed by a coating of PEI to increase the relative and absolute QY to 0.63 and 0.62, respectively.

### 3.3. Investigation of two-photon properties using a self-developed femtosecond Ti-sapphire laser optical system

To develop a high-QY contrast agent, this study leveraged multiphoton properties and maximized deep-tissue penetration by employing an irradiation source with wavelengths shifting from the visible range to the NIR-I and NIR-II windows that create low photodamage, scattering, energy absorption, and background tissue autofluorescence. The detection limit was enhanced using a nonlinear, coupled multiphoton laser that penetrated less than 1 mm into tissue. This laser was non-invasive in terms of subcellular features. The intensity of two-photon luminescence (TPL), which is non-linear, is proportional to the cross-section of TPE, the square of the excitation power, and the PL QY (Ouzounov et al., 2017). The materials and methods section (Supplementary Material) presents the calculations for the laser power. TPE (159.32 nJ pixel<sup>-1</sup>, 1.5932 mW) was performed using a self-developed femtosecond Ti-sapphire laser optical system (80-MHz repetition rate; Mai Tai optical parametric oscillators, Spectra-Physics, USA, Scheme S1); the *z*-axis resolution (full width at half maximum, FWHM) was 948.35 nm (Fig. 2a), and the *x*-*y* axis focal spot was 459.85 nm. These settings helped maintain a low laser power and lengthen the excitation wavelength to the NIR-I or NIR-II region, as well as enhancing TPL visibility in two-photon imaging (TPI). In deep-tissue NIR investigations, as illustrated in Fig. 2b and Fig. S8a, the most efficient excitation wavelength in TPE was 980 nm, probably because of the involved interband transitions (Ouzounov et al., 2017). This phenomenon is also called two-photon absorption (TPA). Since the observed intrinsic- and defect-state emissions may have involved a PL mechanism, the amino-N-GQD-polymer composite could be used as a contrast probe under TPE. Figure 2c illustrates the amino-N-GQD-polymer composites indicating strong TPL under the TPE of a short-pulse laser. The amino-N-GQD-polymer composite had a TPL spectrum ranging from 500 to 900 nm that peaked at 845 nm (Ex: 980 nm); this corresponded to 846 nm in the emission spectrum under OPE [continuous-wave (CW) laser diode, Ex: 808 nm; Fig. 2d]. A two-photon process was observed with an exponent of approximately 2.00 (Fig. 2e; approximately 1.99 for amino-N-GQD, Fig. S6b), and the PL intensity quadratically depended on the TPE excitation power (Ex: 980 nm) (Kuo et al., 2020). A large cross-section is useful for the monitoring of molecular events and the amino-N-GQD-polymer composites had an estimated absolute TPE cross-section of 60,158 Goepfert–Mayer units (GM; 1 GM = 10<sup>-50</sup> cm<sup>4</sup> s photon<sup>-1</sup>) and was Rhodamine B according to Kuo et al. (2020) (Table 1; Fig. S9 and Table S1). The

amino-N-GQD had an estimated cross-section of 51,031 GM. An extremely low TPE cross-section generally results in a weak TPL intensity. In the present study, the amino-N-GQD-polymer composites' absolute TPE cross-section was at least 443 times those of conventional fluorophores and semiconductor quantum dots (Table 1). Since intrinsic fluorophores and enhanced localized excitation power result in a high QY as well as a large TPE cross-section, they can enhance TPL signals (Ouzounov et al., 2017). The observed lifetimes of the amino-N-GQD-PSS-PEI samples were 0.15, 0.87, and 3.87 ns. The amino-N-GQD-polymer composites had an estimated average lifetime of 1.00 ns, determined using time-correlated single-photon counting and a triple-exponential function to fit the results (Fig. 2f and Table 2), compared to the estimated average lifetime of 1.28 ns for amino-N-GQDs (Table 2; Fig. S8c). The increase in TPL occurred because of enlargements in the QY, and the TPL could be confirmed according to lifetime variations. The radiative decay rate was  $6.30 \times 10^8 \text{ s}^{-1}$  for the amino-N-GQD-polymer composites, and the nonradiative decay rate was  $3.70 \times 10^8 \text{ s}^{-1}$ ; the ratio of these two rates was approximately 1.70. The amino-N-GQDs had corresponding rates of  $2.19 \times 10^8$  and  $5.63 \times 10^8 \text{ s}^{-1}$  and a ratio of  $\sim 0.39$ , which was notably smaller. After TPE, as the QY increased and the lifetime decreased, the amino-N-GQD-polymer composites primarily decayed through the radiative pathway.

### 3.4. Stability, physiological, and reactive oxygen species (ROS) assays

A contrast agent for the bioimaging of pathological changes or diseased tissue should be biocompatible, photostable, and efficient uptake in acidic environments. The uptake was assessed in A431 skin cancer cells using a conjugated anti-epidermal growth factor receptor antibody (Ab<sub>EGFR</sub>) and amino-N-GQD-PSS-PEI to increase the efficiency and specificity of targeting cells whose surfaces overexpressed epidermal growth factor receptor. As presented in Fig. 3a, there was a burst uptake rate of 51.5% for the basic material within 5 h but the initial profile of material-Ab<sub>EGFR</sub> was approximately 84.8%. Since the antibody had highly specific binding, considerable quantities of material-Ab<sub>EGFR</sub> were either adsorbed onto the surface or incorporated into the cells, thereby affecting the burst and rapid rates. The sites that could absorb material-Ab<sub>EGFR</sub> were saturated from the 4th to the 10th h, therefore the uptake rate plateaued but the rate for the material alone did not plateau until the 8th hour. The amino-N-GQDs (Fig. S8d) behaved similarly to the amino-N-GQD-polymer composites. Although both amino-N-GQD-polymer composite-Ab<sub>EGFR</sub> and amino-N-GQD-Ab<sub>EGFR</sub> demonstrated acceptable biocompatibility (Fig. S8e) and favorable stability in physiological environments (Table S2), the cancer cells subjected to TPE exhibited non-ROS-dependent oxidative stress (Tables S3-S5), which was consistent with the singlet oxygen (<sup>1</sup>O<sub>2</sub>) phosphorescence signal from the amino-N-GQD-polymer composites at 1270 nm (Fig. 3b). Additionally, the estimated amino-N-GQD and amino-N-GQD-polymer <sup>1</sup>O<sub>2</sub> QYs ( $\Phi_{\Delta}$ ) were 0.52 and 0.03, respectively [for reference,  $\Phi_{\Delta} = 0.64$  for *meso*-tetra(4-sulfonatophenyl)porphine dihydrochloride in deuterium oxide (Kuo et al., 2022)], therefore the polymer coating prevented the release of the generated

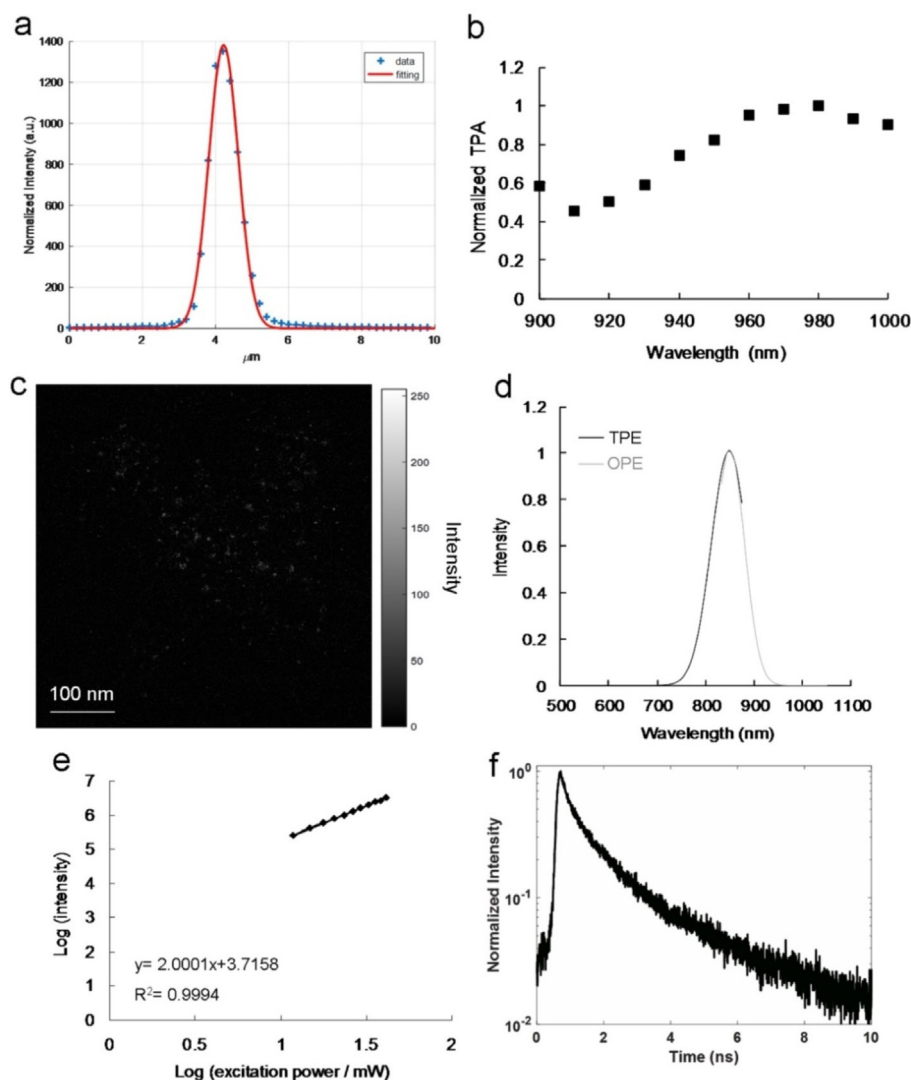


**Fig. 2** (a) Laser system  $z$ -axis resolution (FWHM;  $\sim 948.35$  nm; fitting function: Gaussian function). The second harmonic generation signal at different positions was measured through a  $z$ -axis scan of a thin gold film. (b) Amino-N-GQD-polymer composites relative TPA spectra. TPE executed at  $118.32$  nJ pixel $^{-1}$  as a function of wavelength (900–1000 nm) was applied for signal monitoring. (c) Amino-N-GQD-polymer composite TPL image (gray level) obtained through TPE at  $118.32$  nJ pixel $^{-1}$  over 30 scans (total effective exposure time:  $\sim 0.20$  s; scan rate:  $6.80$  ms per scan; scan area:  $200 \times 200 \mu\text{m}^2$ ; calculations presented in the materials and methods section, Supplementary Material). (d) Relative PL spectra of amino-N-GQD-polymer composites exposed to  $10$  mW of excited power under OPE (808-nm CW laser diode; Ex/Em:  $808$  nm/  $846$  nm) and TPE (Ex/Em:  $980$  nm/  $845$  nm; power:  $159.32$  nJ pixel $^{-1}$ ; cutoff:  $900$  nm, as executed using cascading filters). (e) TPL intensity dependence (slope:  $2.00$ ) on the amino-N-GQD-polymer composites' excitation power (logarithm); TPE exposure from  $1183.20$  to  $4732.80$  nJ pixel $^{-1}$  (Ex:  $980$  nm;  $R^2 > 0.999$ ). (f) Material time-resolved room-temperature PL decay profiles (Ex:  $980$  nm; power:  $118.32$  nJ pixel $^{-1}$ ). Material dose:  $1 \mu\text{g mL}^{-1}$ .

ROS, so amino-N-GQD-polymers are more suitable than amino-N-GQDs for imaging probes. After the TPL intensity was determined in 6 min (approximately 52,941 scans) of photoexcitation under TPE ( $4732.80$  nJ pixel $^{-1}$ ; Ex:  $980$  nm), sustainable two-photon photostability and a diminished photobleaching effect were observed for the amino-N-GQD-polymer composites (Fig. 3c). The amino-N-GQD-polymer composites' two-photon characteristics are effective for producing marked changes in two-photon inquiries. In acidic environments (e.g., specimens with cancerous cells), the amino-N-GQD-polymer composites could produce high TPL because they had suitable photostability (Fig. 3d).

### 3.5. Deep and noninvasive TPI observed under the TPE wavelength in the NIR-I or NIR-II window

The amino-N-GQDs had a favorable absolute cross-section, absorption, luminescence, QY, and stability under TPE, thus are suitable contrast agents for the non-invasive detection of deep and nonplanar biological specimens at a TPE wavelength in the NIR-I or NIR-II range. As indicated in Fig. 2b and Fig. S8a, a  $980$ -nm excitation wavelength resulted in the most intense TPL signal from amino-N-GQD-polymer composites, and the  $980$ -nm excitation wavelength resulted in the most intense two-photon autofluorescence (TPAF) signal in specific

**Table 1** TPE cross-section of materials (Ex: 800 nm).

Reference	Integrated emission intensity (counts)		Action cross-section ( $\eta\sigma$ )
Rhodamine B <sup>a</sup>	58.94		20.01
Sample	Integrated emission intensity (counts)	Relative quantum yield ( $\eta$ )	Absolute cross-section ( $\sigma$ )
amino-N-GQD	42087.50	0.30	51030.76
amino-N-GQD-polymer composites	111634.52	0.63	60158.21
Alexa 488	81.78	0.92 <sup>b</sup>	30.18
Alexa 594	263.44	0.66 <sup>b</sup>	135.51
525 Qdot ITK	98234.67	0.81 <sup>b</sup>	41173.40
Carboxyl quantum dots (Q21341MP)			

<sup>a</sup> Rhodamine B was selected as the standard reference for the cross-section, and the relevant calculations are presented in the materials and methods section.

<sup>b</sup> Information was obtained from the official website of Thermo Fisher Scientific (Waltham, MA, USA).

**Table 2** Lifetimes and parameters obtained through time-correlated single-photon counting, which involved TPE with a triple-exponential fitting function and emission monitoring at 980 nm.

	3 exp fitting model: $(a_0 \cdot \exp(a_1x) + a_2 \cdot \exp(a_3x) + a_4 \cdot \exp(a_5x) + a_6)$							lifetime1	lifetime2	lifetime3	average lifetime (ns)
	a0	a1	a2	a3	a4	a5	a6				
amino-N-GQD	183.03	-4.89	292.47	-1.01	105.19	-0.26	1.50	0.21	0.99	3.92	1.28
amino-N-GQD-polymer composites	275.15	-6.70	369.34	-1.16	98.05	-0.26	-0.82	0.15	0.87	3.87	1.00

cancer cells. These cancer cells have biological molecules that caused the signal in the TPAF image (Feng et al., 2021, Kuo et al., 2020). *In vivo* assays cannot be performed using our developed, optically inverted microscopy system, so cells were embedded in a collagen matrix resembling epithelial tissue to simulate TPL in deep tissue through TPI (Ouzounov et al., 2017) with TPL images of the material-Ab<sub>EGFR</sub>-treated cells recorded at depths of 120–240  $\mu\text{m}$  under TPE (Ex: 980 nm; Fig. 4). To achieve a constant TPL intensity, both the amino-N-GQD-Ab<sub>EGFR</sub>-treated cells (Figs. 4a–c) and amino-N-GQD-polymer composite-Ab<sub>EGFR</sub>-treated cells (Figs. 4d–f) in TPI required TPE power increases of 35% and 27%, respectively, after 160 scans (total effective exposure time:  $\sim 1.09$  s, 6.80 ms per scan,  $200 \times 200\text{-}\mu\text{m}^2$  scan area; calculations presented in the materials and methods section, Supplementary Material). The detection power for the TPI of the cells treated with amino-N-GQD-polymer composite-Ab<sub>EGFR</sub> was nearly 8, 8.5, and 9 times less than the emission of the cells treated with amino-N-GQD-Ab<sub>EGFR</sub>. Conversely, the cells treated with amino-N-GQD-polymer composites demonstrated notably less polymer attachment to their surfaces and remarkably little polymer internalization (800 scans, approximately 5.44 s of total exposure time, Fig. 4g). Emission intensity is quadratically dependent on incident power, therefore, for equal excitation power levels, the excitation ratio between the TPI modalities of the cells treated with the amino-N-GQDs and amino-N-GQD-polymer composites-Ab<sub>EGFR</sub> was estimated to be 64, 72, and 91 times brighter than the standard. In addition, for TPE in unlabeled cells, the TPAF imaging

(800 scans, approximately 5.44 s of total exposure time, Figs. 4h–j) that demonstrated the same intrinsic fluorophore signal level for the cancerous cells was related to a total power  $1938.33 \text{ nJ pixel}^{-1}$  (Fig. 4j). However, the TPE power decreased to  $23.93 \text{ nJ pixel}^{-1}$  for the cells treated with amino-N-GQD-polymer composites-Ab<sub>EGFR</sub> (Fig. 4f) and was approximately 81 times less than the power of the TPAF imaging of the unlabeled cells but reached a similar collected intensity (Fig. 4j), indicating that the TPL intensity was approximately 6561 times brighter than that of the TPAF imaging of the unlabeled cells. Even at the 240- $\mu\text{m}$  depth, the TPI was not degraded by spherical aberrations caused by mismatched refractive indices between the sample and the immersion oil under TPE. However, the emissions of the cells treated with amino-N-GQD-polymer composites-Ab<sub>EGFR</sub> at an excitation power of 10 mW under OPE (808 nm CW laser diode) were not effectively detected when the depth was consistently increased (Figs. 4k–m). Furthermore, the lens working distance enabled imaging tissue phantoms of both TPL and TPAF. TPL images of the cells treated with material-Ab<sub>EGFR</sub> and unlabeled-cell TPAF images were captured at depths from 270 to 330  $\mu\text{m}$  (at increments of 30  $\mu\text{m}$ ) under TPE (Ex: 980 nm) (Fig. 5). The TPI emissions presented in Figs. 5a–c and 5d–f were not detected at a power level of  $23.93 \text{ nJ pixel}^{-1}$  (160 scans, total exposure time of  $\sim 1.09$  s) or  $1938.33 \text{ nJ pixel}^{-1}$  (800 scans, total exposure time of  $\sim 5.44$  s). However, images at depths  $> 270 \mu\text{m}$  contained spherical aberrations that severely degraded their quality; these aberrations were caused by the mismatched refractive indices

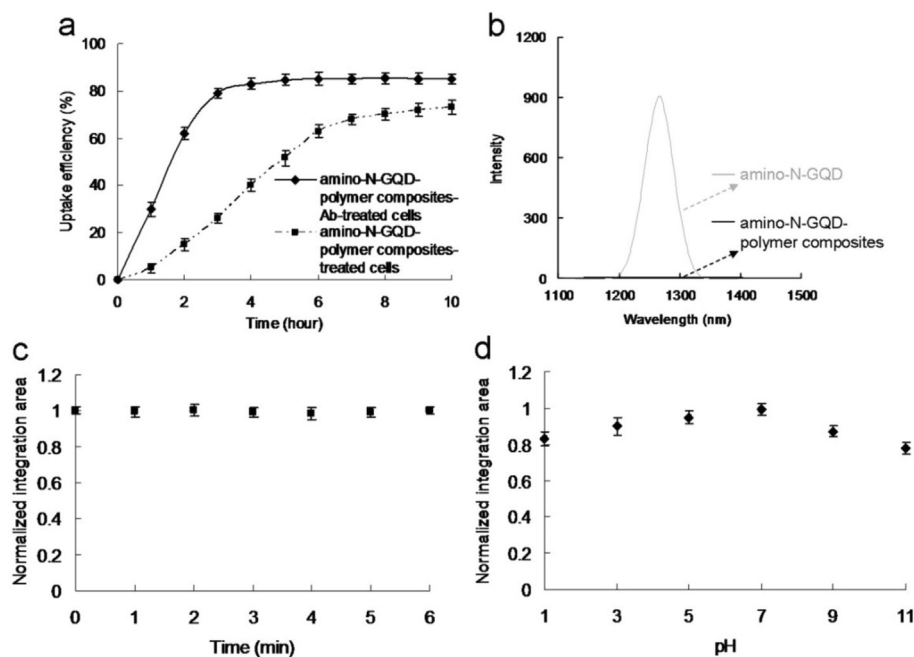


**Fig. 3** (a) Uptake of amino-N-GQD-polymer composites with and without Ab<sub>EGFR</sub> by A431 cells at 37 °C. (b) PL spectral measurements of amino-N-GQDs and amino-N-GQD-polymer composites at 1270 nm. (c) Two-photon stability of amino-N-GQD-polymer composites. TPL spectrum of the material under TPE at 4732.80 nJ pixel<sup>-1</sup> for detecting materials with irradiation. Peak located at 845 nm under TPE (Ex: 980 nm). The integrated area maintained nearly constant relative intensity as a function of TPE time (0–6 min; number of scans: approximately 0–52941 scans) and at 500–900 nm, demonstrating high photostability. (d) Amino-N-GQD-polymer composite TPL emissions under 4732.80 nJ pixel<sup>-1</sup> TPE (Ex: 980 nm) were pH dependent. Integrated-area TPL intensity as a function of pH (1–11) from 500 to 900 nm. The amino-N-GQD-polymer composites' TPL intensity values were high from pH 1 to 11. Material dose: 1 μg mL<sup>-1</sup>. Data presented as mean ± SD (*n* = 6).

of the aqueous sample and immersion oil as well as the objective used, detection efficiency, and maximal *z* depth of the optical laser system.

#### 4. Discussion

GQDs are attracting more interest due to their benign, abundant, and inexpensive nature. Carbon is commonly a black material and until recently, was generally considered to have low solubility in water and weak fluorescence (Torres et al., 2017), thus tiny GQDs have recently attracted increasing attention because of their strong fluorescence, for which they are referred to as fluorescent carbon. Compared to traditional organic dyes, photoluminescent GQDs are superior in terms of high aqueous solubility, robust chemical inertness, easy functionalization, high resistance to photobleaching, low toxicity, and good biocompatibility, thus they have potential applications in biological labeling, bio-imaging, and drug delivery (Gong et al., 2019). Of particular interest and significance is the recent finding that GQDs can exhibit PL emission from visible to NIR spectral region under light excitation. However, it should be noted that NIR PL emission of GQDs excited by NIR is particularly significant and useful for *in vivo* bionanotechnology because of the transparency of body tissues in the NIR for water window (Feng et al., 2021). Interestingly, the PL from GQDs can be quenched by either electron acceptor or electron donor molecules in solution, indicating that photoexcited GQDs are excellent electron donors and accep-

tors. The interesting photoinduced electron transfer properties of GQDs should offer exciting opportunities for light energy conversion, photovoltaic devices, and related applications. GQDs can also be used as nanoprobe for promising and sensitive detection (Sun et al., 2020).

Atom doping facilitates the modification of the intrinsic properties of GQDs, including their surface features, local chemical features, and electronic characteristics, thus producing GQDs with unique quantum confinement and edge effects, which may be completely distinct from those of unaltered GQDs (i.e., sp<sup>2</sup>-bonded GQDs) (Zhu et al., 2017). The production of N-GQDs, which can engender heterocyclic aromatic compounds, may alter the chemical composition of GQDs and adjust the GQD band gap to improve their electrocatalytic, electrochemical, and photochemical properties. Consequently, achieving tunable luminescence in bioimaging applications becomes feasible. Moreover, the use of primary amine molecules (i.e., amino functionalization) for chemical modification causes substantial electron donation, which considerably enhances the electronic characteristics of N-GQDs (Li et al., 2019). The efficiency of intersystem crossing is sufficient to compensate for the internal conversion in states with identical multiplicity levels because N-doped and amino-functionalized GQDs (i.e., amino-N-GQDs) exhibit singlet-triplet splitting, thus the fluorescence emissions may increase (Lee et al., 2023).

However, it has been demonstrated that C-based nanomaterials with oligomeric poly(propionylethyleneimine-co-ethyleneimine) and poly(ethylene glycol) diamine surface conjuga-

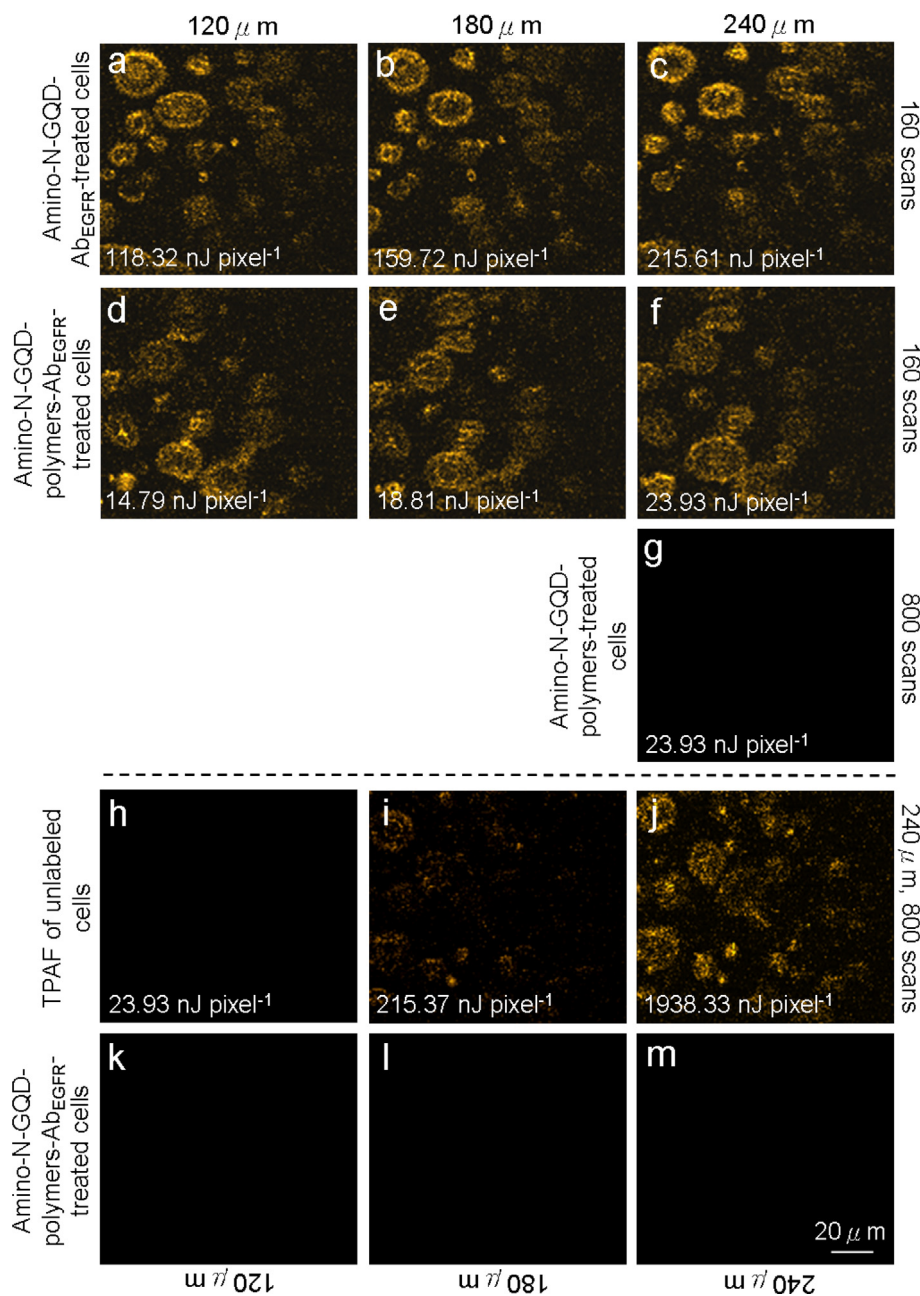


**Fig. 4** TPL images (gray level) of (a–c) cells treated with amino-N-GQD-Ab<sub>EGFR</sub> recorded at depths of 120–240 μm with total TPE power increments of 118.32 to 215.61 nJ pixel<sup>-1</sup> over 160 scans. (d–f) Cells treated with amino-N-GQD-polymer composites-Ab<sub>EGFR</sub> subjected to TPE at 14.79–23.93 nJ pixel<sup>-1</sup> over 160 scans. (g) Cells treated with amino-N-GQD-polymer composites without antibody coating were indistinct under TPE at 23.93 nJ pixel<sup>-1</sup> (800 scans) at a 240-μm depth. TPAF images of unlabeled (untreated) cells under TPE at (h) 23.93, (i) 215.61, and (j) 1938.33 nJ pixel<sup>-1</sup> (number of scans: 800; EX: 980 nm). (k–m) Images of amino-N-GQD-polymer composites-Ab<sub>EGFR</sub>-treated cells at a constant depth and 10-mW excitation power under OPE (808 nm CW laser diode). Material dose: 1 μg mL<sup>-1</sup>.

tion exhibit a substantially higher QY and fluorescence than other C-based nanomaterials because the conjugation impedes the nonradiative recombination of localized hole-electron pairs into sp<sup>2</sup> clusters, enhances the surface integrity of the π-electron network, and improves the electronic properties and optical characteristics (Yang et al., 2021). Non-radiative traps and structures exist on the C core of a crystalline-sorted GQD-based material with multiple crystalline layers (Tao et al., 2020;

Tao et al., 2022). Moreover, surface coating with N-doped, amino-functionalized, and N, S-atom-containing polymers (amino-N-GQD-based material-polymer) improved the cooperative effect (among the electrons captured by the new surface states) on the heteroatom-doped materials due to the crosslink-enhanced emission (Sun et al., 2020). Specifically, the heteroatom dopants and linked polymer coatings diminished rotation and vibration and thus enhanced the PL (Ghazali et al., 2023).

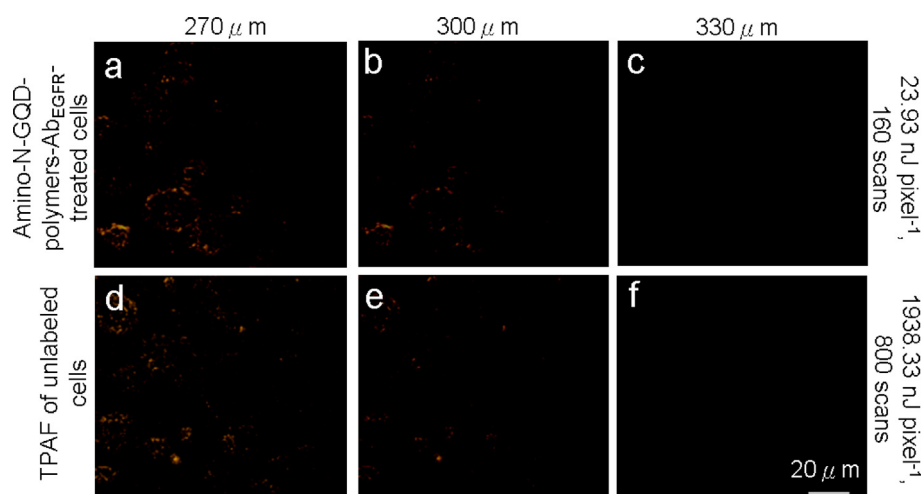


**Fig. 5** (a–c) TPL images (pseudo-color level) of cells treated with amino-N-GQD-polymer composites and (d–f) TPAF images of unlabeled cells at various depths (with a consistent depth increment from 270 to 330  $\mu\text{m}$ ) at power levels of 23.93 and 1938.33  $\text{nJ pixel}^{-1}$  (160 and 800 scans, respectively) under TPE (Ex: 980 nm). Material dose:  $1 \mu\text{g mL}^{-1}$ .

This enhanced the frequency of radiative recombination, thus engendering quantum confinement effects and inducing enhanced PL QY. Accordingly, the surface coating improved the surface of the amino-N-GQDs by strengthening the quantum confinement of their emissive energy. These results reveal that the exceptionally bright, highly photostable, and sorted amino-N-GQD-PSS-PEI materials prepared in this study are suitable for use as fluorescence probes in biological and biomedical applications for target analysis.

Multiphoton laser microscopy (also known as two-photon laser microscopy) uses localized “nonlinear” excitation to excite fluorescence within only a thin raster-scanned plane. Two-photon laser microscopy has been used in various imaging studies (Periasamy et al., 2020) and is typically coupled with NIR laser excitation to capitalize on the inherent maximum tissue transmission for bioimaging because NIR has the advantages of slight scattering, low energy absorption, optimal irradiation penetration, and reduced photobleaching of specimens (Chia et al., 2021). The coupling of two-photon laser microscopy with NIR laser excitation has become the preferred technique for fluorescence microscopy in thick tissue and deeper biological specimens (Pinkard et al., 2021) and has been extensively applied in other photoexcitation tracking and diagnosis (Jones et al., 2018). Moreover, because of its ultra-low energy and short photoexcitation, two-photon laser microscopy is an alternative bioimaging approach for sensitive detection (Streich et al., 2021).

Consequently, it is expected that the N-GQD-polymers, which generate non-reactive oxygen species-dependent oxidative stress, act as two-photon contrast agents for biological applications and for obtaining images in deeper biological specimens and tissues in the human body in the future.

## 5. Conclusion

The trapped emissive energy on surfaces of materials (amino-N-GQDs coated with PSS and PEI to form amino-N-GQD-PSS-PEI or amino-N-GQD-polymer composites) is quantum confined by connected polymers when such polymers contain doped N and S atoms, resulting in notable two-photon characteristics and high PL QY values. Amino-

N-GQD-polymer composites generated non-ROS-dependent oxidative stress in cells and have the potential for application as contrast probes. Ab<sub>EGFR</sub> antibody amino-N-GQD-polymer composite conjugate-labeled cancer cells allowed molecule-specific imaging with high signal-to-noise ratios deep in a tissue phantom. When imaging depths must be selected according to the balance between high power and tissue damage prevention, the brightness supplied by amino-N-GQD-polymer composites might increase the feasible imaging depth. Moreover, the TPI capabilities can be expanded by the amino-N-GQD-polymer composites to facilitate non-invasive imaging detection of diverse new molecular signatures excited in NIR-I or NIR-II window using our femtosecond Ti-sapphire laser optical system. The present findings indicate the feasibility of future biological applications, particularly those that require capturing images deep within interior tissues and biological specimens.

## CRedit authorship contribution statement

**Wen-Shuo Kuo:** Conceptualization, Data curation, Formal analysis, Investigation, Methodology, Resources, Software, Supervision, Validation. **Yen-Sung Lin:** Conceptualization, Data curation, Formal analysis, Investigation, Methodology, Resources, Software, Supervision, Validation. **Meng-Zhi Han:** Conceptualization, Data curation, Formal analysis, Investigation, Methodology, Resources, Software, Supervision, Validation. **Hao-Yu Chuang:** Data curation, Formal analysis, Funding acquisition, Investigation, Methodology, Project administration, Resources, Software, Validation. **Ping-Ching Wu:** Data curation, Formal analysis, Funding acquisition, Investigation, Methodology, Project administration, Resources, Software, Validation. **Chia-Yuan Chang:** Data curation, Formal analysis, Funding acquisition, Investigation, Methodology, Project administration, Resources, Software, Validation. **Jiu-Yao Wang:** Data curation, Formal analysis, Funding acquisition, Investigation, Methodology, Project administration, Resources, Software, Validation. **Hui-Fan Kao:** Data curation, Formal analysis, Funding acquisition, Investigation, Methodology, Project administration, Resources, Software, Validation. **Shih-Wen Tseng:** Data curation, Formal analysis, Funding acquisition, Investigation,

Methodology, Project administration, Resources, Software, Validation. **Sheng-Han Lin:** Conceptualization, Data curation, Formal analysis, Investigation, Methodology, Resources, Software, Validation. **Po-Lan Su:** Conceptualization, Data curation, Formal analysis, Investigation, Methodology, Resources, Software, Validation. **Chan-Chi Chang:** Conceptualization, Data curation, Formal analysis, Investigation, Methodology, Resources, Software, Validation.

### Declaration of Competing Interest

The authors declare that they have no known competing financial interests or personal relationships that could have appeared to influence the work reported in this paper.

### Acknowledgements

Experiments and data analysis were performed in part through the use of the Medical Research Core Facilities Center, Office of Research & Development at China medical University, Taichung, Taiwan (R.O.C.). The authors also gratefully acknowledged the use of [EM000800] JEOL JEM-2100F Cs STEM and [ESCA003700] PHI VersaProbe 4 XPS, the Core Facility Center of National Cheng Kung University, Taiwan.

### Funding

This research was supported by the Center for Allergy Immunology and Microbiome (AIM), China Medical University Children's Hospital/China Medical University Hospital, China Medical University, Taiwan (1JA8; DMR-112-043; DMR-111-215; DMR-HHC-111-5; DMR-112-205); An Nan Hospital, China Medical University, Taiwan (ANHRF111-12); National Science and Technology Council (NSTC), Taiwan (NSTC 111-2113-M-039-003-MY2; NSTC 110-2314-B-039-056-MY3); National Cheng Kung University Hospital and E-Da Hospital Bilateral Research Grant, Taiwan (NCKUEDA11208).

### Appendix A. Supplementary material

Supplementary data to this article can be found online at <https://doi.org/10.1016/j.arabjc.2023.105188>.

### References

- Barman, M.K., Patra, A., 2018. Current status and prospects on chemical structure driven photoluminescence behaviour of carbon dots. *J. Photochem. Photobiol. C: Photochem. Rev.* 37, 1–22. <https://doi.org/10.1016/j.jphotochemrev.2018.08.001>.
- Chia, Z.C., Yang, L.X., Cheng, T.Y., Chen, Y.J., Cheng, H.L., Hsu, F.T., Wang, Y.J., Chen, Y.Y., Huang, T.C., Fang, Y.S., Huang, C.C., 2021. In situ formation of Au-glycopolymers nanoparticles for surface-enhanced Raman scattering-based biosensing and single-cell immunity. *ACS Appl. Mater. Interfaces* 13 (44), 52995–52307. <https://doi.org/10.1021/acsami.1c13647>.
- Dsouza, S.D., Buerkle, M., Brunet, P., Maddi, C., Padmanaban, D.B., Morelli, A., Payam, A.F., Maguire, P., Mariotti, D., Svrcek, 2021. The importance of surface states in N-doped carbon quantum dots. *Carbon* 183, 1–11. <https://doi.org/10.1016/j.carbon.2021.06.088>
- Feng, Z., Tang, T., Wu, T., Yu, X., Zhang, Y., Wang, M., Zhang, J., Ying, Y., Chen, S., Zhou, J., Fan, X., Zhang, D., Li, S., Zhang, M., Qian, . Perfecting and extending the near-infrared imaging window. *Light Sci. Appl.* 10 (1), 197. <https://doi.org/10.1038/s41377-021-00628-0>.
- Ghazali, S.A.I.S.M., Fatimah, I., Izaddin, S.A., Zamli, Z.N., Zulkuffli, N.N., Adam, N., 2023. Graphene quantum dots: A comprehensive overview. *Open Chem.* 21 (1), 20220285. <https://doi.org/10.1515/chem-2022-0285>.
- Gong, P., Sun, L., Wang, F., Liu, X., Yan, Z., Wang, M., Zhang, L., Tian, Z., Liu, Z., You, J., 2019. Highly fluorescent N-doped carbon dots with two-photon emission for ultrasensitive detection of tumor marker and visual monitor anticancer drug loading and delivery. *Chem. Eng. J.* 356, 994–1002. <https://doi.org/10.1016/j.cej.2018.09.100>.
- Hummers, W.S., Offeman, R.E., 1958. Preparation of graphitic oxide. *J. Am. Chem. Soc.* 80 (6), 1339. <https://doi.org/10.1021/ja01539a017>.
- Jones, J.D., Ramser, H.E., Woessner, A.E., Quinn, K.P., 2018. In vivo multiphoton microscopy detects longitudinal metabolic changes associated with delayed skin wound healing. *Commun. Biol.* 1, 198. <https://doi.org/10.1038/s42003-018-0206-4>.
- Kang, J.W., Kang, D.H., 2021. Effect of amino acid-derived nitrogen and/or sulfur doping on the visible-light-driven antimicrobial activity of carbon quantum dots: A comparative study. *Chem. Eng. J.* 420, (1). <https://doi.org/10.1016/j.cej.2021.129990>
- Kumar, P., Dua, S., Kaur, R., Kumar, M., Bhatt, G., 2022. A review on advancements in carbon quantum dots and their application in photovoltaics. *RSC Adv.* 12 (8), 4714–4759. <https://doi.org/10.1039/d1ra08452f>.
- Kuo, W.S., Chang, C.Y., Liu, J.H., So, E.C., Wu, P.C., 2020. Two-photon photoexcited photodynamic therapy with water-soluble fullereneol serving as the highly effective two-photon photosensitizer against multidrug-resistant bacteria. *Inter. J. Nanomed.* 15, 6813–6825. <https://doi.org/10.2147/IJN.S236897>.
- Kuo, W.S., Shen, X.C., Chang, C.Y., Kao, H.F., Lin, S.H., Wang, J.Y., Wu, P.C., 2020. Multiplexed graphene quantum dots with excitation-wavelength-independent photoluminescence, as two-photon probes, and in ultraviolet-near infrared bioimaging. *ACS Nano* 14 (9), 11502–11509. <https://doi.org/10.1021/acsnano.0c03915>.
- Kuo, W.S., Wu, P.C., Chang, C.Y., Chang, C.Y., Wang, J.Y., Chen, P.C., Hsieh, M.S., Lin, S.H., Cheng, J.S., Chou, Y.T., 2022. Graphene near infrared-I/II probe in two-photon excitation-wavelength-independent photoluminescence and photoinactivation. *Carbon* 193, 205–215. <https://doi.org/10.1016/j.carbon.2022.03.019>.
- Lee, S., Lee, J., Jeon, S., 2023. Aggregation-induced emission of matrix-free graphene quantum dots via selective edge functionalization of rotor molecules. *Sci. Adv.* 9 (7), eade2585. <https://doi.org/10.1016/sciafv.ade2585>.
- Lee, C.W., Wu, P.C., Hsu, I.L., Liu, T.M., Chong, W.H., Wu, C.H., Hsieh, T.Y., Guo, L.Z., Tsao, Y., Wu, P.T., Yu, J., Tsai, P.J., Huang, H.S., Chuang, Y.C., Huang, C.C., 2019. New templated Ostwald ripening process of mesostructured FeOOH for third-harmonic generation bioimaging. *Small* 15 (20), 1805086. <https://doi.org/10.1002/sml.201805086>.
- Li, S., Li, C., Su, B., Hu, M.Z., Gao, X., Gao, C., 2019. Amino-functionalized graphene quantum dots (aGQDs)-embedded thin film nanocomposites for solvent resistant nanofiltration (SRNF) membranes based on covalent interactions. *J. Membr. Sci.* 588., <https://doi.org/10.1016/j.memsci.2019.117212>
- Li, Y., Zhao, T., Cheng, H., Hu, Y., Shi, G., Dai, L., Qu, L., 2012. Nitrogen-doped graphene quantum dots with oxygen-rich functional groups. *J. Am. Chem. Soc.* 134 (1), 15–18. <https://doi.org/10.1021/ja206030c>.
- Liao, M.Y., Wu, C.H., Lai, P.S., Yu, J., Lin, H.P., Liu, T.M., 2012. Surface state mediated NIR two-photon fluorescence of iron oxides for nonlinear optical microscopy. *Adv. Func. Mater.* 23 (16), 2044–2051. <https://doi.org/10.1002/adfm.201202676>.

- Ouzounov, D.G., Wang, T., Wang, M., Feng, D.D., Horton, N.G., Cruz-Hernández, J.C., Cheng, Y.T., Reimer, J., Tolias, A.S., Nishimura, N., Xu, C., 2017. In vivo three-photon imaging of activity of GCaMP6-labeled neurons deep in intact mouse brain. *Nat. Methods* 14 (4), 388–390. <https://doi.org/10.1038/nmeth.4183>.
- Periasamy, A., König, K., So, P., 2020. Special section guest editorial: Thirty years of multiphoton microscopy in the biomedical sciences. *J. Biomed. Opt.* 25, (1). <https://doi.org/10.1117/1.JBO.25.1.014501014501>.
- Pinkard, H., Baghdassarian, H., Mujal, A., Roberts, E., Hu, K.H., Friedman, D.H., Malenica, I., Shagam, T., Fries, A., Corbin, K., Krummel, M.W., Waller, L., 2021. Learned adaptive multiphoton illumination microscopy for large-scale immune response imaging. *Nat. Commun.* 12, 1916. <https://doi.org/10.1038/s41467-021-22246-5>.
- Ruhlandt et al., Anderson, M., Jensen, N., Gregor, I., Jakobs, S., Enderlein, J., Chizhik, A.I., 2020. Absolute quantum yield measurements of fluorescent proteins using a plasmonic nanocavity. *Commun. Biol.* 3, 627. <https://doi.org/10.1038/s42003-020-01316-2>
- Sheka, E.F., Golubev, Y.A., Popova, N.A., 2020. Graphene domain signature of Raman spectra of  $sp^2$  amorphous carbons. *Nanomaterials* 10, 2021. <https://doi.org/10.3390/nano10102021>.
- Streich, L., Boffi, J.C., Wang, L., Alhalaseh, K., Barbieri, M., Rehm, R., Deivasigamani, S., Gross, C.T.T., Agarwal, A., Prevedel, R., 2021. High-resolution structural and functional deep brain imaging using adaptive optics three-photon microscopy. *Nat. Methods* 18, 1253–1258. <https://doi.org/10.1038/s41592-021-01257-6>.
- Sun, Z., Fang, S., Hu, Y., H., 2020. 3D graphene materials: from understanding to design and synthesis control. *Chem. Rev.* 120 (18), 10336–10453. <https://doi.org/acs.chemrev.0c00083>.
- Tao, S., Zhu, S., Feng, T., Zhang, C., 2020. Crosslink-enhanced emission effect on luminescence in polymers: Advances and perspectives. *Angew. Chem. Int. Ed.* 59 (25), 9826–9840. <https://doi.org/10.1002/anie.201916591>.
- Tao, S., Zhou, C., Kang, C., Zhu, S., Feng, T., Zhang, S.T., Ding, Z., Zheng, C., Xia, C., Yang, B., 2022. Confined-domain crosslink-enhanced emission effect in carbonized polymers dots. *Ligh. Sci. Appl.* 11, 56. <https://doi.org/10.1038/s41377-022-00745-4>.
- Torres, T., 2017. Graphene chemistry. *Chem. Soc. Rev.* 46 (15), 4385–4386. <https://doi.org/10.1039/c7cs90061a>.
- Wu, J.B., Lin, M.L., Cong, X., Liu, H.N., Tan, P.H., 2018. Raman spectroscopy of graphene-based materials and its applications in related devices. *Chem. Soc. Rev.* 47 (5), 1822–1873. <https://doi.org/10.1039/c6cs00915h>.
- Yang, P.C., Ting, Y.X., Gu, S., Gandomi, Y.A., Li, J., Hsieh C.T., 2021. Effect of solvent on fluorescence emission from polyethylene glycol-coated grapebe quantum dots under blue light illumination. *Naomaterials* 11 (6), 1383. <http://doi.org/10.3390/nano11061383>.
- Yang, L.X., Liu, Y.C., Cho, C.H., Chen, Y.R., Yang, C.S., Lu, Y.L., Zhang, Z., Tasi, Y.T., Chin, Y.C., Yu, J., Pan, H.M., Jiang, W.R., Chia, Z.C., Huang, W.S., Chiu, Y.L., Sun, C.K., Huang, Y.T., Chen, L.M., Wong, K.T., Huang, H.M., Chen, C.H., Chang, Y.J., Huang, C.C., Liu, T.M., 2022. A universal strategy for the fabrication of single-photon and multiphoton NIR nanoparticles by loading organic dyes into water-soluble polymer nanosponges. *J. Nanobiotechnol.* 20, 311. <https://doi.org/10.1186/s12951-022-01515-5>.
- Zhang, L., Yang, A., Ruan, C., Jiang, B.P., Guo, X., Liang, H., Kuo, W.S., Shen, X.C., 2023. Copper-nitrogen-coordinated carbon dots: transformable phototheranostics from precise PTT/PDT to post-treatment imaging-guided PDT for residual tumor cells. *ACS Appl. Mater. Interfaces* 15 (2), 3253–3265. <https://doi.org/10.1021/acami.2c17525>.
- Zhu, S., Song, Y., Wang, J., Wan, H., Zhang, Y., Ning, Y., Yang, B., 2017. Photoluminescence mechanism in graphene quantum dots: Quantum confinement effect and surface/edge state. *Nanotoday* 13, 10–14. <http://doi.org/10.1016/j.nantod.2016.12.006>.